



Delft University of Technology

## Systematic DEM calibration of two-component mixtures using AI-accelerated surrogate models

Hadi, Ahmed; Pang, Yusong; Schott, Dingena

### DOI

[10.1016/j.powtec.2025.121190](https://doi.org/10.1016/j.powtec.2025.121190)

### Publication date

2025

### Document Version

Final published version

### Published in

Powder Technology

### Citation (APA)

Hadi, A., Pang, Y., & Schott, D. (2025). Systematic DEM calibration of two-component mixtures using AI-accelerated surrogate models. *Powder Technology*, 464, Article 121190.  
<https://doi.org/10.1016/j.powtec.2025.121190>

### Important note

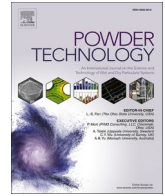
To cite this publication, please use the final published version (if applicable).  
Please check the document version above.

### Copyright

Other than for strictly personal use, it is not permitted to download, forward or distribute the text or part of it, without the consent of the author(s) and/or copyright holder(s), unless the work is under an open content license such as Creative Commons.

### Takedown policy

Please contact us and provide details if you believe this document breaches copyrights.  
We will remove access to the work immediately and investigate your claim.



# Systematic DEM calibration of two-component mixtures using AI-accelerated surrogate models

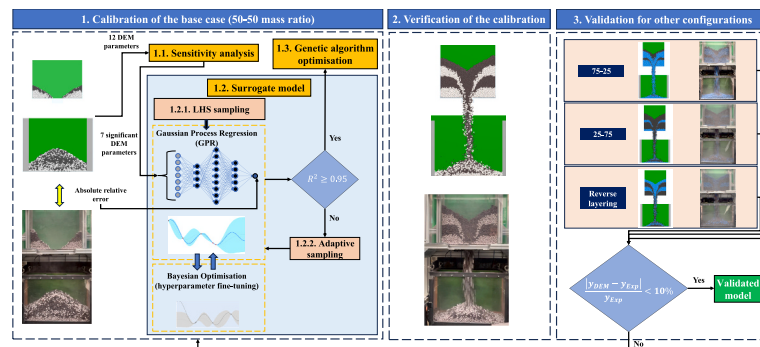
Ahmed Hadi<sup>\*</sup>, Yusong Pang, Dingena Schott

Department of Maritime and Transport Technology, Faculty of Mechanical Engineering, Delft University of Technology, Delft 2628CD, the Netherlands

## HIGHLIGHTS

- Efficient DEM calibration via screening, surrogate modelling, and optimisation.
- Accurate surrogate modelling using GPR and adaptive sampling.
- Calibrated parameters for a single mass ratio remain valid for other ratios.
- Average values for interaction parameters between components yield accurate results.
- For segregation, DEM stochasticity dominates the effect of varying DEM parameters.

## GRAPHICAL ABSTRACT



## ARTICLE INFO

### Keywords:

Granular materials  
Discrete element method  
DEM calibration  
Granular mixtures  
Machine learning  
Adaptive sampling  
Surrogate models

## ABSTRACT

Calibration of discrete element method (DEM) models is crucial for the realistic simulation of granular materials. However, it remains a challenging task, especially for multi-component mixtures due to their higher complexity and larger number of parameters involved. This study presents a systematic and computationally efficient calibration framework designed to address these challenges, focusing on pellet-sinter mixtures, as a representative case of two-component mixtures commonly used in blast furnace steelmaking. The framework integrates sensitivity analysis, machine learning-based surrogate modelling with adaptive sampling, and genetic algorithm-driven optimisation techniques to minimise the number of required DEM simulations. Using this approach, we achieved a high-accuracy surrogate model ( $R^2 = 0.95$ ) for seven DEM parameters with only 110 data points, highlighting the efficiency and robustness of the framework. These parameters were successfully calibrated with a relative error of less than 2 %. Moreover, the calibrated parameters for the base case (i.e., 50–50 pellet-sinter mass ratio) remained valid across different mass ratios and layering orders, eliminating the need for recalibration. Overall, the proposed framework offers a reliable, cost-effective, and adaptable solution for DEM calibration of two-component mixtures. Its flexibility and efficiency make it a promising tool for extending to more complex systems, facilitating the development of DEM models for a wide range of industrial applications involving granular mixtures.

<sup>\*</sup> Corresponding author.

E-mail address: [A.H.Hadi-1@tudelft.nl](mailto:A.H.Hadi-1@tudelft.nl) (A. Hadi).

## 1. Introduction

Granular materials are the second most handled materials in industry after water [1], making it important to understand their behaviour for optimising industrial processes. The Discrete Element Method (DEM), first introduced by Cundall and Strack [2], has become a widely used computational tool for simulating granular materials. DEM provides particle-level insights into complex granular flows that are virtually impossible to obtain through experiments [3–8]. However, the reliability of DEM outcomes heavily depends on the proper determination of input parameters, which remains a significant challenge.

Various approaches have been employed in past studies to determine the DEM parameters, which can be categorised into trial-and-error methods and systematic calibration approaches [9]. Trial-and-error, although still widely used [10,11], are highly inefficient, subjective, and often fail to produce optimal parameter sets [12].

In contrast, systematic calibration approaches offer more efficient alternatives by employing optimisation algorithms and can be divided into two distinct groups [9]. The first group couples optimisation with costly DEM simulations, where each parameter set update requires running a full DEM simulation to evaluate the objective function. Several studies have used this approach, using optimisation techniques such as particle swarm optimisation [13], and genetic algorithms [14–16]. However, the approach of this group suffers from the high computational cost associated with the large number of DEM simulations required.

The second group is surrogate-based DEM calibration. A Surrogate model (SM), also known as a metamodel, is an approximation of a more complex and computationally demanding model, such as DEM [17]. SMs are especially suitable for DEM calibration as they are effective at finding a global optimum, handling parameter constraints, and are computationally efficient [12]. In this approach, an SM is first developed to capture the relationship between DEM parameters and outputs. The outputs typically represent the differences between experimental and DEM measurements of key performance indicators (KPIs), which are minimised during the calibration process. The SM is then used during the optimisation process to identify the optimal (i.e., calibrated) parameter sets. The key advantage of this approach is the significant reduction in computational time, as the fast surrogate model replaces costly DEM simulations during optimisation [12].

With the rapid advancement of AI, machine learning (ML)-based surrogate modelling has gained popularity in recent years. In the context of DEM calibration, several studies have explored the use of various ML models to create surrogate models. These include Gaussian process regression (GPR) and Kriging [12,18–21], multi-objective reinforcement learning [22], Bayesian filtering [23,24], multi-variate regression analysis [25], neural networks [26], and random forest (RF) [27].

Despite the advancements in DEM calibration approaches, several challenges remain. First, while SMs can significantly accelerate the optimisation process, the efficient development of accurate SMs is still a big challenge [9]. Second, most studies develop SMs for a limited subset of DEM parameters. A key drawback is that the selection of the parameters to be calibrated is often subjective, which can lead to overlooking other potentially significant parameters. Third, the majority of existing studies focus on the calibration of single-component systems, while DEM calibration for multi-component mixtures—despite being common in industrial applications—is rare [28–30]. Multi-component mixtures introduce additional challenges, including a larger set of DEM parameters for individual materials as well as their interactions, the need to account for varying component ratios, and changes in layering order.

This study aims to address these challenges by developing a systematic and efficient calibration framework based on ML-based surrogate models for DEM modelling of multi-component mixtures. As a case study, we apply the framework to the mixture of iron ore pellets and sinter, which is used in blast furnace steelmaking. The proposed

framework integrates sensitivity analysis, efficient surrogate modelling, and optimisation techniques to calibrate the DEM parameters effectively and efficiently. Furthermore, the robustness and generalisability of the calibrated parameters are validated across different mass ratios and layering orders of the mixture.

The structure of the paper is as follows. Section 2 describes the experimental setup, procedures, and results. In Section 3, the DEM model and the proposed systematic calibration framework are outlined. Finally, the paper concludes with key findings and suggestions for future research endeavours.

## 2. Experiments

This section covers the materials, experimental setup, and procedure, as well as the methodology for measuring the key performance indicators (KPIs) and their corresponding results.

### 2.1. Materials

Fig. 1 shows iron ore pellets and sinter used in this study. As shown, they have similar colours, making them difficult to distinguish during experiments. To address this issue, we coated the pellets with a thin layer of water-based white/blue paint.<sup>1</sup> In our previous work, we performed a comparative analysis of the angle of repose (AoR) in the ledge test using both painted and unpainted particles [28]. The results showed no significant difference in the AoR, which validates the use of painted particles in our experiments.

We measured the size distribution of both pellets and sinter using sieves. The particle density ( $\rho_p$ ) was also determined by measuring the weight of a number of particles with known volume and dividing their weight by volume. The results of the particle size distribution and particle density measurements are reported in Table 1.

### 2.2. Draw down test

The draw down test has been widely used in previous studies to calibrate DEM models [32,33]. Fig. 2 schematically illustrates the draw down test setup used in this study. The setup consists of an upper and lower box positioned vertically, with load cells attached to the frame supporting the upper box. The outlet of the upper box is initially sealed with a plate, which can be released using electromagnets.

The procedure for each test is as follows. First, the upper box is filled with 40 kg of materials (Fig. 3(a)). Next, the magnetic outlet of the upper

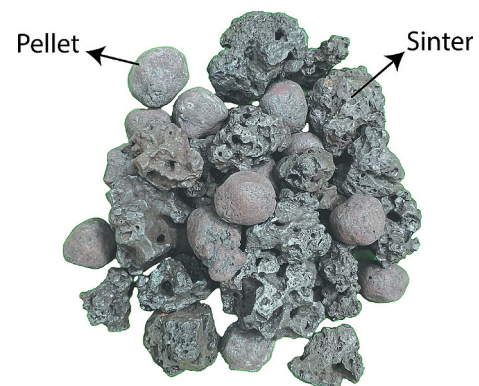


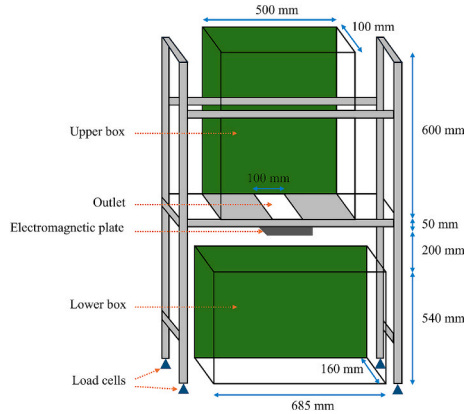
Fig. 1. A mixture of iron ore pellets and sinter (from [31]).

<sup>1</sup> Initially, we used white paint, but later discovered that blue is a better choice because it makes the “Lab” colour space easier and more reliable to use.

**Table 1**

The results of the particle size distribution and particle density measurements.

| Material properties        | Pellet                                 | Sinter                                 |
|----------------------------|--|--|
| Particle size distribution | 10–12.5 (mm): 48 %                     | 5.6–8 (mm): 36.37 %                    |
|                            | 12.5–16 (mm): 52 %                     | 8–10 (mm): 23.13 %                     |
|                            |  | 10–12.5 (mm): 17.61 %                  |
|                            |  | 12.5–16 (mm): 13.45 %                  |
|                            |  | 16–20 (mm): 5.08 %                     |
| Solid density ( $\rho_s$ ) | $3602.4 \pm 61.7$ (kg/m <sup>3</sup> ) | 20–25 (mm): 4.36 %                     |
|                            |  | $3449.0 \pm 34.0$ (kg/m <sup>3</sup> ) |

**Fig. 2.** Schematic of the draw down test setup used in this study with detailed dimensions.

box is manually removed, allowing the material to discharge into the lower box (Fig. 3(b)). During discharging, load cells continuously record the remaining weight of the material in the upper box at a frequency of 50 Hz (every 0.02 s). This data is used to calculate the mass flow rate and the mass of the materials collected in the lower box. Once the discharge is finished, a photo is captured using a camera to measure the shear angle and the angle of repose (Fig. 3(c)). We performed experiments for three different mass ratios of pellet-sinter: 50–50, 75–25 and 25–75. Additionally, for 50–50 ratio, we conducted a set of experiments with reverse layering (i.e. sinter-pellets-sinter-pellets from bottom to top).

In addition to these measurements, we evaluated the segregation of pellets and sinter in the lower box. As shown in Fig. 3(a), the upper box was filled with four alternating layers of pellets and sinter. We chose this

layering approach instead of mixing materials to keep control over the initial configuration and remove the uncertainty about the segregation produced while filling the upper box [34]. Moreover, previous studies have shown that the initial configuration of materials significantly influences downstream segregation [31,35]. Therefore, ensuring a consistent initial configuration is crucial, especially when the experiments are used for calibrating or verifying segregation in a discrete element method (DEM) model. The same photo used to measure the AoR was analysed to evaluate the segregation in the lower box.

These measurements highlight the versatility of the draw down test in measuring multiple key performance indicators (KPIs) in a single experiment. These KPIs include the shear angle in the upper box, the AoR and segregation in the lower box, the mass flow rate, and the total mass discharged into the lower box.

### 2.3. Measurement of KPIs

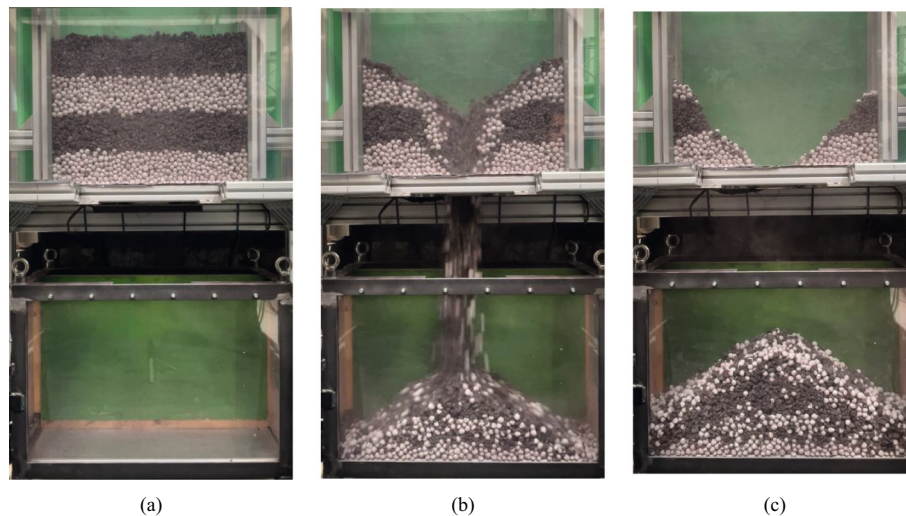
#### 2.3.1. Shear angle and angle of repose

We used MATLAB's image processing toolbox to measure the shear angle and the angle of repose following the same methodology outlined in our previous work [28]. First, the raw image was pre-processed which involves cropping the image to focus on the region of interest (ROI), removing the background, and inserting an artificial background for improved contrast, as shown in Fig. 4(a). Next, the pre-processed image was binarized (Fig. 4(b)) and the edge of the particles was extracted (Fig. 4(c)). Finally, a linear line was fitted to the detected edge, the slope of which was calculated to determine the shear angle or the angle of repose.

We considered the average of two measured angles in the upper box (shear angle (left) and (right) in (Fig. 4) as the shear angle. For the angle of repose in the lower box, the heap was divided at the center (as shown in (Fig. 4(c)), and the angle of repose was determined separately for each half of the heap. The average of these two values was reported as the final angle of repose. While some studies exclude the flattened portion of the heap from the calculation of the angle of repose [32,36], we used the entire heap profile for consistency. This is because there is no clear rule for determining the extent of the flattened portion to exclude.

#### 2.3.2. Segregation in the lower box

We employed image analysis to evaluate segregation in the lower box. Compared to physical sampling, this method is non-intrusive and avoids the challenge of separating the components for materials overlapping in size [37,38]. To quantify segregation, we used the same pre-

**Fig. 3.** The draw down test procedure. (a) upper box filled with materials where white and dark grey particles represent pellets and sinter, respectively, (b) discharging of materials into the lower box, and (c) the end of a test.



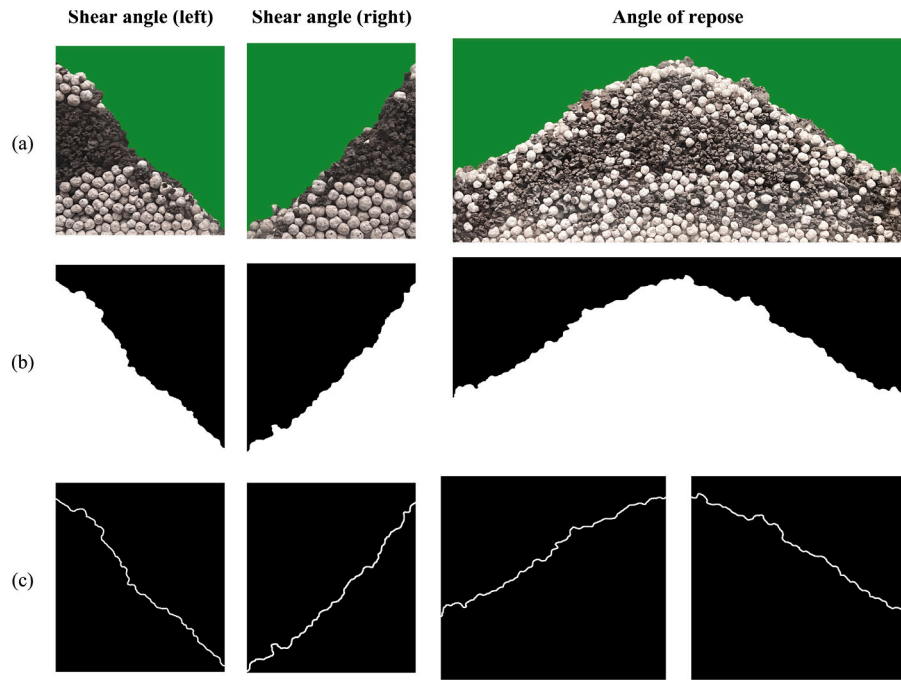


**Fig. 4.** The process of measuring the shear angle or the angle of repose in an image: (a) the pre-processed image, (b) the binarized image, and (c) the extracted edge.

processed image used for calculating the angle of repose (cf. right column in Fig. 4(a)). Next, we segmented the image using the colour thresholding capabilities of MATLAB's image processing toolbox to create two separate figures: one where white pixels represent pellets (Fig. 5(b), right) and the other where white pixels represent sinter particles (Fig. 5(b), left).

Next, we divided the image into slices, either vertically (Fig. 5(c)) or horizontally (Fig. 5(d)), to measure segregation in the respective direction. We evaluated the effect of the slice size on segregation measurements, resulting in 6 and 3 slices for horizontal and vertical directions, respectively. Then, we measured the pixel fraction of each

component ( $C_{ik}$ ) in each slice as:

$$C_{ik} = \frac{N_{ik}}{\sum_{i=1}^n N_{ik}} \quad (1)$$

where  $N_{ik}$  is the number of pixels for component  $i$  in the  $k$ th slice and  $n$  is the total number of components (pellets and sinter). The average ( $\mu_i$ ) and standard deviation ( $\sigma_i$ ) of pixel fractions are calculated across all slices for each component. Finally, the Relative Standard Deviation (RSD), used as the segregation index, was calculated as:

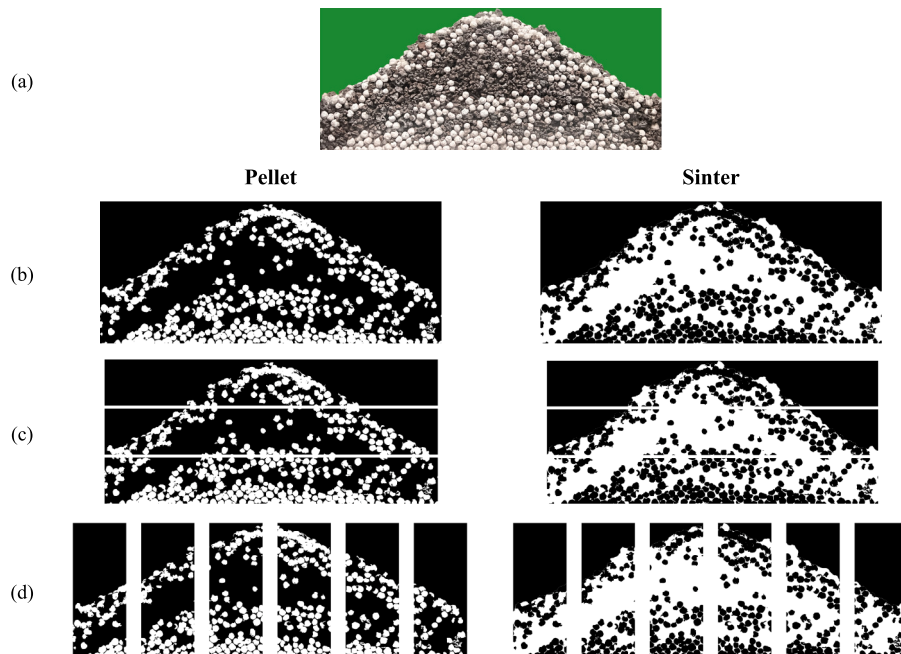


**Fig. 5.** The process of image segmentation and slicing for quantifying segregation: (a) the original pre-processed image, (b) the binary images, and the sliced images used for calculating (c) vertical segregation and (d) horizontal segregation.

$$RSD_i = \frac{\sigma_i}{\mu_i} \quad (2)$$

where higher RSD denotes higher segregation.

### 2.3.3. Mass flow rate and mass in the lower box

The load cell data recorded during discharge was used to calculate the mass flow rate. As the raw data contained significant noise, a Gaussian filter was applied to smooth the data. Fig. 6 shows an example of the mass in the upper box plotted against time. The steady mass flow rate was determined from the slope of the nearly linear segment between 0.5 and 2.0 s, illustrated by the shaded area in Fig. 6. Additionally, the discharged mass in the lower box was determined by subtracting the remaining mass in the upper box from the total initial mass of the material.

### 2.3.4. Results of the experiments

Table 2 summarises the results of the measurements mentioned above for all tested pellets-sinter mass ratios as well as the reverse layering case. For the complete experimental data, readers are referred to the published dataset [39].

The results show that increasing the sinter ratio in the mixture leads to a higher angle of repose and shear angle, which aligns with the findings of Chakrabarty et al. [40]. This effect is expected due to the highly irregular shape of sinter particles compared to the near-spherical shape of pellets (see Fig. 1). Also, this study is one of the first of its kind to investigate the impact of layering order, showing that reversing the order slightly reduces the shear angle compared to the normal 50–50 case, while the angle of repose remains largely unchanged.

The mass flow rate remains relatively constant across different mass ratios and layering orders, indicating that these factors do not significantly influence discharge behaviour under the tested conditions. The mass discharged into the lower box shows a negative correlation with the shear angle, as stated by Wasserfall et al. [32].

For segregation, interpreting the effect of mass ratio using RSD is challenging. Since the RSD formula (Eq. (2)) normalises the standard deviation by the mean, and the mean is directly linked to the mass ratio, no meaningful conclusions can be drawn about the influence of the mass ratio on segregation [31]. In the reverse layering case, lower horizontal and higher vertical segregation were observed, which is in agreement with the findings of our previous study [31].

## 3. Discrete element method (DEM) model

The materials and experimental setup are modelled using the

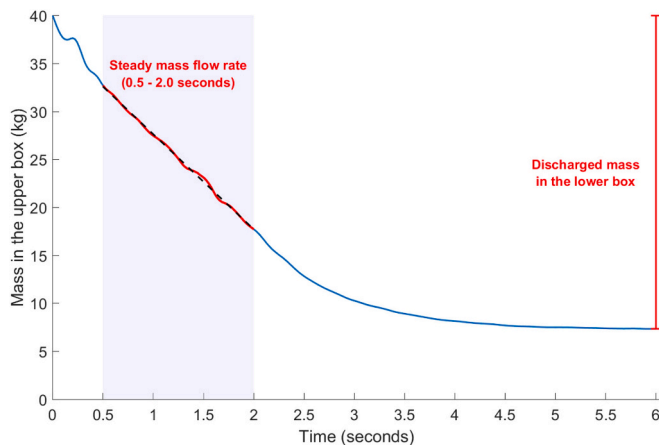


Fig. 6. An example of the mass in the upper box plotted against time, illustrating the calculation of the mass flow rate and the discharged mass in the lower box.

Discrete Element Method (DEM). Before presenting the model setup in detail, we first introduce the calibration approach.

### 3.1. Systematic calibration/verification framework

Fig. 7 illustrates an overview of the systematic calibration framework adopted in this study. The calibration process starts with the reference case, i.e., 50–50 pellet-sinter mass ratio. Next, the calibrated parameters are validated by testing their applicability to the other two mass ratios: 75–25 and 25–75. These steps are further explained in the following subsections.

### 3.2. Model setup

#### 3.2.1. Contact model

We chose the Hertz-Mindlin contact model with an elastic-plastic spring-dashpot rolling friction model (type C, as classified by Ai et al. [41]) for the DEM model. This contact model has been successfully employed in previous studies on pellets and sinter [28,40,42]. Fig. 8 schematically illustrates the interaction forces between two particles in the DEM model. For a detailed explanation of the related equations, readers are referred to the relevant literature [40–43].

#### 3.2.2. Fixed DEM parameters

We obtained the intrinsic material properties, including the shear modulus and Poisson's ratio, from relevant literature, as listed in Table 3 [40,42]. Pellets were modelled as spheres due to their nearly spherical shape (see Fig. 1). However, sinter particles, which have highly irregular shapes (see Fig. 1), were represented using a three-sphere clump shape, as shown in Table 3. This shape has been successfully used in previous studies to model sinter particles [40,44].

For particle size distribution and particle density, we used the experimentally measured values reported in Table 1.

#### 3.2.3. DEM parameters to calibrate

All DEM parameters, excluding the fixed parameters listed in Table 1, were considered for calibration in this study. This included both particle-particle and particle-geometry interaction parameters. However, the pellet-sinter interaction parameters were not directly calibrated. Instead, these parameters were defined as the average of the pellet-pellet and sinter-sinter interaction parameters, following a similar approach used in a previous study on the calibration of pellet-sinter mixtures [40]. To establish a reference case model for time step and sensitivity analyses, we adopted particle-particle and particle-geometry interaction parameters from a similar study on pellet-sinter mixtures [40].

#### 3.2.4. Time step analysis

Selecting the appropriate time step in DEM is a crucial aspect of the calibration process, which ensures numerical stability, computational efficiency, and accurate results [18,45]. A widely used approach is to consider the time step as a fraction of Rayleigh time step calculated as:

$$\Delta t = \frac{\pi r \sqrt{\frac{\rho}{G}}}{0.1631\nu + 0.8766} \quad (3)$$

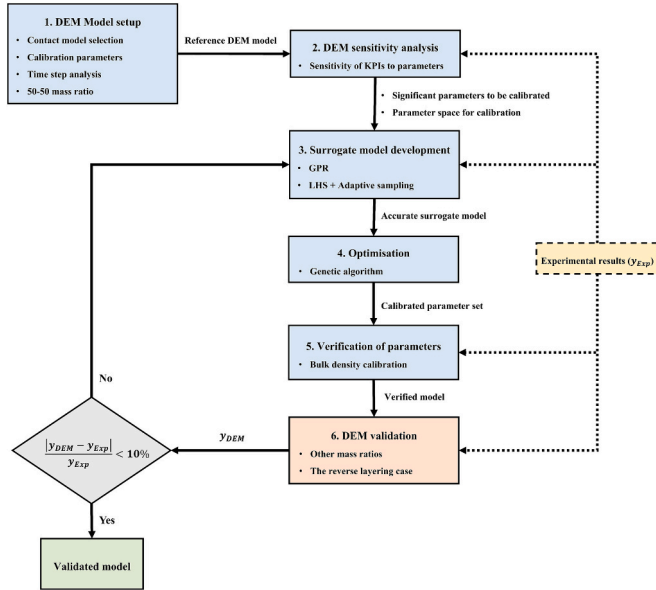
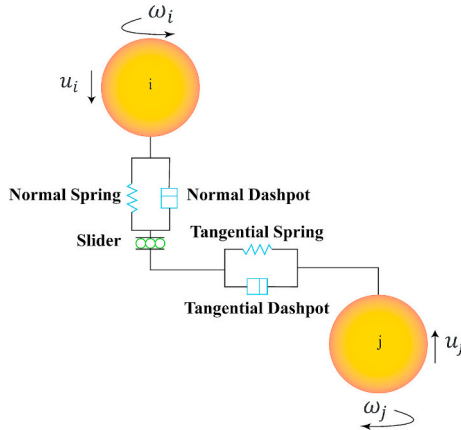
where  $r$ ,  $\rho$ ,  $G$ ,  $\nu$  are the minimum radius, particle density, shear modulus, and Poisson's ratio of particles, respectively. We varied the time step from 5 % to 40 % to examine its effect on all KPIs. The results are presented in Fig. 9 (a-f). It is important to note that we employed the same methodology used in experiments to measure KPIs in the DEM simulations. This consistency allowed for a direct and accurate comparison between the DEM results and the experimental measurements.

We used two criteria to determine the appropriate time step: (1) relatively stable KPI values up to the selected time step and (2) low standard deviation, which indicates high reproducibility. Fig. 9 shows that most KPIs, including mass flow rate, mass in the lower box, shear



**Table 2**

Results of KPIs measured in the experiments. The values are presented with their 95 % confidence intervals.

| Pellets-sinter mass ratio | Angle of repose (°) | Shear angle (°) | Mass flow rate (kg/s) | Mass in the lower box (kg) | Segregation (RSD) |               |
|---------------------------|---------------------|-----------------|-----------------------|----------------------------|-------------------|---------------|
|                           |                     |                 |                       |                            | Vertical          | Horizontal    |
| 50–50                     | 29.47 ± 0.48        | 42.51 ± 1.62    | 10.29 ± 0.35          | 32.32 ± 0.55               | 0.264 ± 0.07      | 0.121 ± 0.04  |
| 75–25                     | 28.55 ± 0.65        | 39.03 ± 1.49    | 10.29 ± 0.1           | 33.09 ± 0.12               | 0.151 ± 0.03      | 0.082 ± 0.02  |
| 25–75                     | 29.63 ± 0.75        | 44.76 ± 1.21    | 10.24 ± 0.45          | 32.00 ± 0.48               | 0.422 ± 0.09      | 0.116 ± 0.025 |
| Reverse layering          | 29.74 ± 0.47        | 40.92 ± 1.55    | 10.39 ± 0.56          | 32.97 ± 0.2                | 0.32 ± 0.03       | 0.112 ± 0.053 |

**Fig. 7.** An overview of the systematic calibration approach adopted in this study.**Fig. 8.** A schematic representation of the interaction forces between particles in DEM (from [31]).**Table 3**

Intrinsic material properties used in DEM simulations.

| DEM Parameter             | Pellet  | Sinter  | Geometry |
|---------------------------|---|---|----------|
| Shear modulus ( $G$ )     | 1e+8 Pa   | 1e+8 Pa   | 2e+11 Pa |
| Poisson's ratio ( $\nu$ ) | 0.25  | 0.25  | 0.3      |
| Particle shape            |  |  | NA       |

angle, and angle of repose, remained stable with low standard deviations up to 15 % of the Rayleigh time step (5.91e-6 s). Especially, for the angle of repose (Fig. 9(a)), there is a drop in value and an increase in standard deviation for time steps greater than 15 %. Therefore, we selected 15 % as it balances computational efficiency, stability, and reproducibility.

### 3.3. Sensitivity analysis

Given the large number of DEM parameters to be calibrated (i.e. 12), we conducted a sensitivity analysis to identify the parameters that significantly influence the KPIs. By focusing the calibration on these significant parameters, the computational expense of the calibration process is significantly reduced [31]. Moreover, the sensitivity analysis helps define the parameter space for calibration, reveal relationships between KPIs, and determine whether the selected KPIs are suitable for calibrating the DEM model.

We employed the definitive screening design (DSD) [46], a design of experiment (DoE) technique, which was successfully used in our previous work to efficiently identify significant parameters [31]. With 12 DEM parameters, the DSD required 29 simulation runs, calculated as  $2k + 5$ , where  $k$  is the number of parameters [47]. The low and high parameter levels for the DSD, shown in Table 4, were set as the reference case values  $\pm 25$  %, with the reference values obtained from [40]. The DSD design is presented in Table A.1 in the appendix.

To account for the stochastic nature of granular systems and DEM, we repeated the DSD analysis five times. Each repetition was analysed independently to identify the significant parameters. The variation in the KPI values can stem from two main sources: (1) the variability introduced by varying the DEM parameters (i.e., DSD design) and (2) the stochastic nature of DEM simulations (i.e., variations across repetitions). To quantify the contribution of each source to the overall variance, we employed the variance decomposition technique [48]. Variance decomposition is based on the law of total variance, which is expressed as:

$$\text{Var}(Y) = \mathbb{E}[\text{Var}(Y|X)] + \text{Var}(\mathbb{E}[Y|X]) \quad (4)$$

where  $Y$  represents the KPI of interest and  $X$  denotes the set of input parameters.  $\mathbb{E}[\text{Var}(Y|X)]$  represents the variance in  $Y$  (i.e., KPI) caused by the stochasticity, while  $\text{Var}(\mathbb{E}[Y|X])$  quantifies the variance in  $Y$  due to varying the DEM parameters. The variance contribution of each source, i.e. the DEM parameters and stochasticity, is calculated as:

$$P = \frac{\text{Var}(\mathbb{E}[Y|X])}{\text{Var}(Y)} \times 100 \quad (5)$$

$$S = \frac{\mathbb{E}[\text{Var}(Y|X)]}{\text{Var}(Y)} \times 100 \quad (6)$$

Fig. 10 presents the variance contribution of DEM parameters and stochasticity for all the KPIs. It reveals that for both horizontal and vertical segregation, the variance caused by DEM stochasticity dominates the variance due to varying the DEM parameters in the DSD design. This indicates that the inherent stochasticity of DEM, related to the initial position and orientation of particles, overshadows the effect of varying parameters on segregation.

Therefore, no meaningful conclusions can be drawn about the

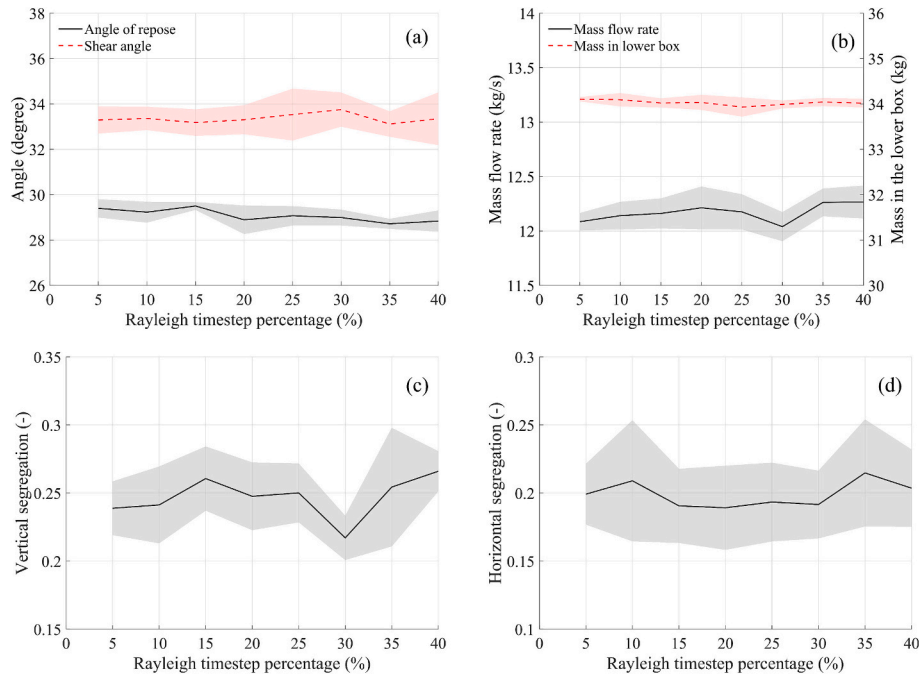


**Fig. 9.** The effect of time step on: a) angle of repose and shear angle, b) mass flow rate and mass in the lower box, c) vertical segregation, and d) horizontal segregation. The lines and shaded areas represent the mean and standard deviation, respectively.

**Table 4**

Low, middle and high levels of DEM parameters used in DSD. ( $\mu_s$  = coefficient of sliding friction,  $\mu_r$  = coefficient of rolling friction,  $C_r$  = coefficient of restitution).

| Parameters      | Low level (-1)     | Middle level (0) [40] | High level (+1) |
|-----------------|--------------------|-----------------------|-----------------|
| Pellet-pellet   | $\mu_{s,pp}$ 0.368 | 0.49                  | 0.613           |
|                 | $\mu_{r,pp}$ 0.045 | 0.06                  | 0.075           |
|                 | $C_{r,pp}$ 0.525   | 0.7                   | 0.875           |
| Sinter-sinter   | $\mu_{s,ss}$ 0.525 | 0.7                   | 0.875           |
|                 | $\mu_{r,ss}$ 0.06  | 0.08                  | 0.1             |
|                 | $C_{r,ss}$ 0.263   | 0.35                  | 0.438           |
| Pellet-geometry | $\mu_{s,pg}$ 0.285 | 0.38                  | 0.475           |
|                 | $\mu_{r,pg}$ 0.045 | 0.06                  | 0.075           |
|                 | $C_{r,pg}$ 0.525   | 0.7                   | 0.875           |
| Sinter-geometry | $\mu_{s,sg}$ 0.285 | 0.38                  | 0.475           |
|                 | $\mu_{r,sg}$ 0.06  | 0.08                  | 0.1             |
|                 | $C_{r,sg}$ 0.3     | 0.4                   | 0.5             |

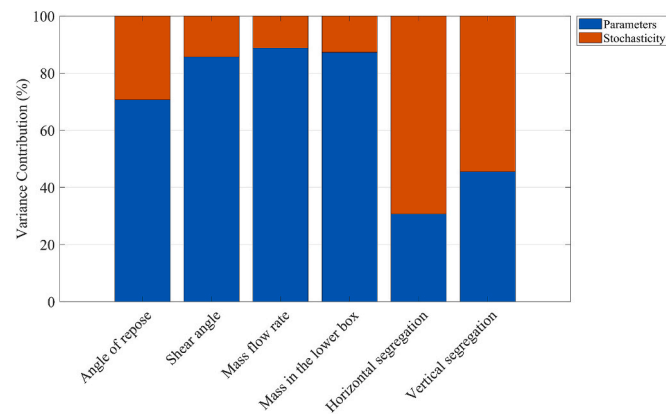


**Fig. 10.** Results of variance contribution of DEM parameters and stochasticity for all the KPIs.

sensitivity of segregation to DEM parameters. As a result, segregation measured in the draw down test cannot be used as a KPI to calibrate the DEM model. Consequently, segregation was excluded from both sensitivity analysis and the DEM calibration process.

For the four remaining KPIs, we used the “Fit Definitive Screening” platform in JMP® Pro software to perform the DoE. Stepwise regression with a  $p$ -value threshold of 0.01, combined with analysis of variance (ANOVA), was applied to identify significant parameters, following our previous study [31]. Since the significance of parameters varied slightly across the five sensitivity analysis repetitions, a parameter was considered significant if it appeared as significant in at least 80 % of the repetitions (i.e., 4 or 5 times) for at least one of the KPIs. The final results of the sensitivity analysis are presented in Table 5, where the significant parameters are shaded to highlight seven parameters selected for calibration.

**Table 5**

Results of the sensitivity analysis, showing the frequency of each parameter appearing as significant across five repetitions, with the significant parameters shaded. (The +/- signs indicate that with an increase in the parameter value, the corresponding KPI increases/decreases.)

| Parameters      | Angle of repose    | Shear angle | Mass flow rate | Mass in the lower box |
|-----------------|--------------------|-------------|----------------|-----------------------|
| Pellet-pellet   | $\mu_{s,pp}$ 0     | 5 (+)       | 1 (-)          | 5 (-)                 |
|                 | $\mu_{r,pp}$ 1 (+) | 5 (+)       | 0              | 5 (-)                 |
|                 | $C_{r,pp}$ 5 (-)   | 1 (+)       | 1 (+)          | 0                     |
| Sinter-sinter   | $\mu_{s,ss}$ 0     | 0           | 5 (-)          | 4 (+)                 |
|                 | $\mu_{r,ss}$ 1 (+) | 1 (+)       | 3 (-)          | 2 (-)                 |
|                 | $C_{r,ss}$ 1 (-)   | 1 (+)       | 1 (+)          | 0                     |
| Pellet-geometry | $\mu_{s,pg}$ 2 (-) | 5 (+)       | 1 (-)          | 4 (-)                 |
|                 | $\mu_{r,pg}$ 1 (-) | 4 (+)       | 1 (+)          | 5 (-)                 |
|                 | $C_{r,pg}$ 1 (-)   | 0           | 1 (+)          | 0                     |
| Sinter-geometry | $\mu_{s,sg}$ 3 (-) | 5 (+)       | 5 (-)          | 5 (-)                 |
|                 | $\mu_{r,sg}$ 1 (-) | 0           | 2 (+)          | 0                     |
|                 | $C_{r,sg}$ 2 (-)   | 0           | 1 (+)          | 1 (+)                 |



### 3.4. Surrogate model development

In this section, we describe the process of establishing a surrogate model (SM) to map the relationship between the significant parameters (the seven parameters shaded in Table 5) and the KPIs.

#### 3.4.1. Parameter space

As mentioned above, one of the advantages of using a screening design is that it helps guide the definition of the parameter space for efficient calibration. To achieve this, we compared the experimental results with the simulation outcomes from the screening runs for each KPI. Fig. 11 shows the results of the screening design compared to the experimental values for each KPI. This comparison, combined with the correlations in Table 5, helped adjust the parameter space of the screening design (Table 4). For example, in Fig. 11(b), the experimental value for the shear angle is higher than all the screening design runs. This indicates that the parameter space for the significant parameters needs to be extended in a way that increases the shear angle. According to Table 5, all significant parameters have a positive correlation (+) with the shear angle. This suggests that their parameter space should be extended to higher values, assuming the correlation remains valid beyond the initial range used in the sensitivity analysis. Repeating this process for the other KPIs, we finalised the parameter space, which is presented in Table 6.

#### 3.4.2. Objective function

With four KPIs to calibrate, there are three potential strategies for building SMs: 1) building a separate SM for each KPI, 2) using multivariate models to create a single SM for all KPIs, or 3) combining all KPIs into a single objective and creating a single SM. Each strategy has its advantages and disadvantages. For simplicity and efficiency, we chose the third strategy. This approach simplifies the SM development process compared to option 2 since it involves using simpler models. Moreover, option 3 is more efficient than 1, as it requires only a single SM. Following the methodology outlined in [12], we combined the KPIs into a single objective using a weighted sum (WS) of the relative error (RE) between the experimental and DEM measurements of KPIs. The WS is calculated as:

**Table 6**

Extended parameter space used for DEM calibration.

| Parameters   | Low band | High band |
|--------------|----------|-----------|
| $\mu_{s,pp}$ | 0.613    | 1.0       |
| $\mu_{r,pp}$ | 0.075    | 0.24      |
| $C_{r,pp}$   | 0.525    | 1.0       |
| $\mu_{s,ss}$ | 0.525    | 1.0       |
| $\mu_{s,pg}$ | 0.285    | 1.0       |
| $\mu_{r,pg}$ | 0.075    | 0.24      |
| $\mu_{s,sg}$ | 0.285    | 1.0       |

$$WS = \sum_{m=1}^M (w_m \cdot RE_m), \text{ with } \sum_{m=1}^M w_m = 1 \quad (7)$$

where  $M$  is the number of KPIs (four in this study),  $w_m$  is the weight for  $m$ th KPI, and  $RE$  is the absolute relative error, computed as:

$$RE = \left| \frac{y_{DEM} - y_{Exp}}{y_{Exp}} \right| \quad (8)$$

Here,  $y_{DEM}$  and  $y_{Exp}$  represent the KPI values obtained from DEM and experiments, respectively. Since all KPIs have equal importance in the calibration process, we assign the same weight ( $w_m$ ) to each of them. The weighted sum (WS) is used as the objective function to be minimised in the calibration process.

#### 3.4.3. Surrogate model training

Fig. 12 provides an overview of the approach used to develop the surrogate model (SM) in this study. For the initial sampling, we used the Latin Hypercube Sampling (LHS) method as it randomly and evenly distributes the points in the parameter space (Table 6). Following the recommendation by Loeppky et al. [49], we sampled 10 points per parameter, resulting in a total of 70 data points. We then ran the DEM simulations with five repetitions for all the points and obtained the value for all the KPIs. These KPI values were subsequently converted into a single objective value, as outlined in Section 3.4.2.

To develop the SM, we used Gaussian Process Regression (GPR), a machine learning model known for effectively capturing complex, non-linear relationships. GPR was specifically chosen because our previous

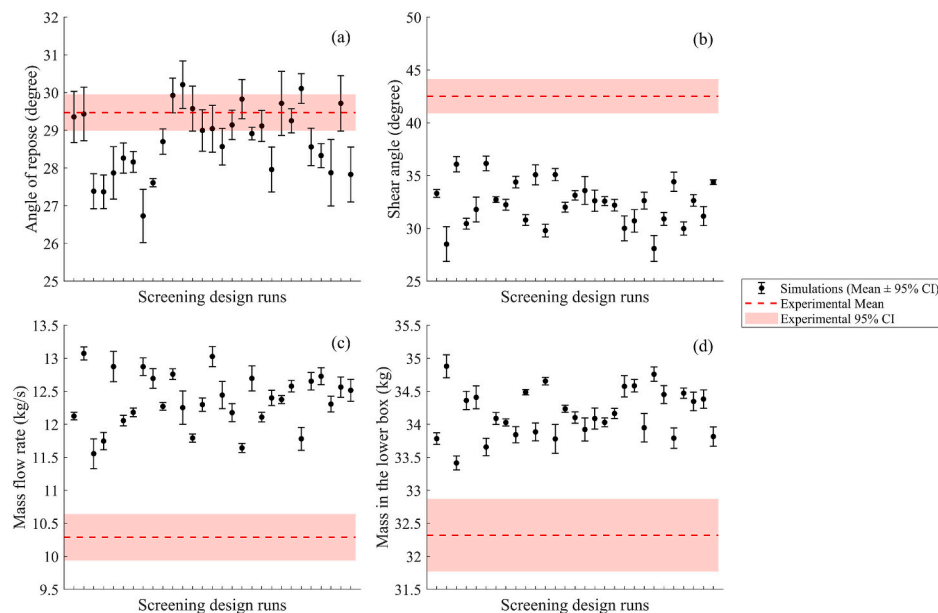


**Fig. 11.** Comparison between sensitivity analysis and experimental results for all KPIs. The differences between the two indicate the need to extend the parameter space.

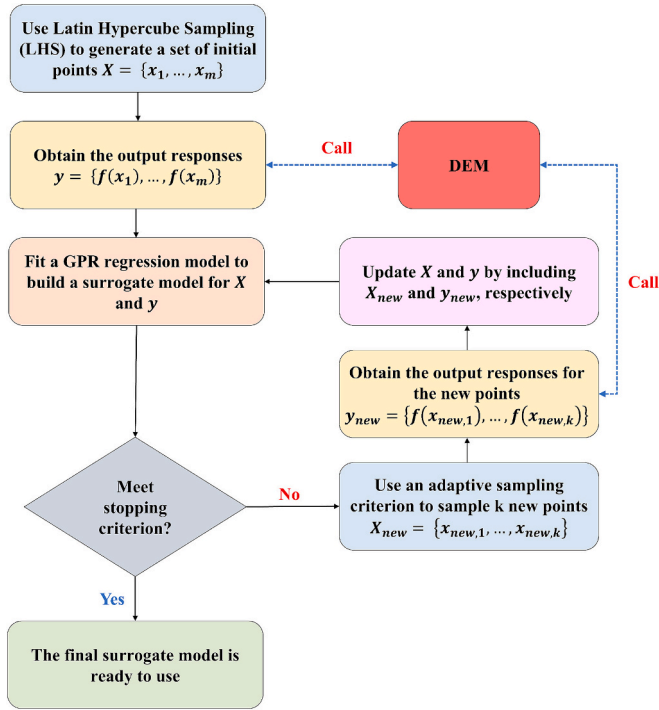


Fig. 12. Flowchart illustrating the surrogate model development approach used in this study, based on [50].

work [9] demonstrated its efficiency in mapping the relationship between DEM parameters and the corresponding response.

Gaussian Process Regression (GPR) is a non-parametric, Bayesian machine learning method that models data using kernel functions. It is particularly effective for small datasets and complex, nonlinear relationships due to its flexibility in hyperparameter tuning. A Gaussian Process (GP) defines a distribution over functions and is fully specified by its mean function,  $\mu(x)$ , and covariance function,  $k(x, x')$ , which together describe the joint Gaussian distribution of random variables.

The GPR model for a given set of input-output pairs  $(x_i, y_i)$  can be represented as:

$$y_i = f(x_i) + \varepsilon_i \quad (9)$$

where  $\varepsilon_i$  is Gaussian noise with zero mean and variance  $\sigma^2$ , denoted as  $\varepsilon_i \sim \mathcal{N}(0, \sigma^2)$ . The goal of GPR is to predict the underlying function  $f$  using a prior distribution:

$$f(x) \sim \mathcal{GP}(\mu(x), k(x, x')) \quad (10)$$

Here, the mean function  $\mu(x)$  is often assumed constant and zero, while the covariance function  $k(x, x')$  captures dependencies between data points.

To predict the output at a new input  $x_*$ , GPR provides a Gaussian posterior distribution:

$$f(x_*) | \mathcal{Y} \sim \mathcal{N}(\mu_*, \sigma_*^2) \quad (11)$$

where the predictive mean ( $\mu_*$ ) and variance ( $\sigma_*^2$ ) are calculated as:

$$\mu_* = \mu(x_*) + \mathcal{K}(x_*)^T (\mathcal{K} + \sigma^2 \mathbf{I}_n)^{-1} (\mathcal{Y} - \mu) \quad (12)$$

$$\sigma_*^2 = k(x_*, x_*) - \mathcal{K}(x_*)^T (\mathcal{K} + \sigma^2 \mathbf{I}_n)^{-1} \mathcal{K}(x_*) \quad (13)$$

In these expressions,  $\mathcal{K}$  is the covariance matrix for the training inputs,  $\mathbf{I}$  is the identity matrix, and  $\mathcal{K}(x_*)$  is the covariance vector between the new input and the training data.

Additionally, the predicted mean can be expressed as a weighted sum

of kernel evaluations:

$$\mathbb{E}(f(x_*) | \mathcal{Y}) = \sum_{i=1}^n k(x_*, x_i) \alpha_i \quad (14)$$

with weights defined as:

$$\begin{bmatrix} \alpha_1 \\ \vdots \\ \alpha_n \end{bmatrix} \triangleq (\mathcal{K} + \sigma^2 \mathbf{I}_n)^{-1} (\mathcal{Y} - \mu) \quad (15)$$

Further details on the kernel functions used are provided in Table A.2 in the appendix.

To avoid overfitting of GPR, we employed k-fold cross-validation combined with Bayesian hyperparameter optimisation (details of which can be found in our previous work [9]). Although various metrics can be used to evaluate the performance of the surrogate model (SM), we focused on the coefficient of determination ( $R^2$ ). After rigorously training the GPR model with an initial set of 70 data points, the model achieved an average cross-validation  $R^2$  value of 0.84, which we considered insufficient for calibration. This suggests that the dataset was too small for the model to fully capture the relationship between the seven DEM parameters and the response (i.e., the weighted sum of the relative errors between experimental and DEM results).

There are two general approaches for expanding the dataset to improve the performance of the SMs [50]: 1) traditional space-filling sampling, and 2) adaptive sampling (also known as active learning) approaches. Compared to the space-filling methods, adaptive sampling methods have a higher potential for improving model performance with fewer points by targeting the most informative areas of the design space [50]. Therefore, we adopted adaptive sampling to expand the dataset in this study.

Specifically, we employed the Expected Improvement (EI) criterion for adaptive sampling, which is well-suited for expensive computational models such as DEM [12,51]. EI balances exploration (sampling in regions of high uncertainty) and exploitation (sampling in regions with promising predicted performance) [50,52]. In this approach, let  $f_{\min}$  denote the best (i.e., smallest) observed function value (or weighted sum of the relative errors) to date. For any candidate point  $x$ , the improvement is defined as:

$$I(x) = \max\{0, f_{\min} - f(x)\} \quad (16)$$

The expected improvement is then given in closed form by:

$$EI(x) = (f_{\min} - \mu(x)) \Phi\left(\frac{f_{\min} - \mu(x)}{\sigma(x)}\right) + \sigma(x) \phi\left(\frac{f_{\min} - \mu(x)}{\sigma(x)}\right) \quad (17)$$

where  $\Phi(\cdot)$  and  $\phi(\cdot)$  are the cumulative distribution function and probability density function of the standard normal distribution, respectively (with the convention that  $EI(x) = 0$  when  $\sigma(x) = 0$ ). The next sample point is selected by maximising the expected improvement:

$$x_{\text{new}} = \operatorname{argmax} EI(x). \quad (18)$$

Adaptive sampling was applied iteratively by adding 10 new data points in each iteration until the stopping criterion was met. An  $R^2$  value of 0.95 was chosen as the stopping criterion to achieve a balance between high model accuracy and computational efficiency.

Fig. 13 shows the actual responses plotted against the surrogate model's predicted values. In the first iteration, adaptive sampling focuses on exploring the parameter space to improve the model's global accuracy. From the second iteration onwards, the sampling strategy shifts towards exploiting regions with lower response values, which are of particular interest for model calibration. The performance of the model across different iterations of the adaptive sampling process is presented in Table 7.

This integrated approach, which combines GPR with an EI-based adaptive sampling strategy, allows us to efficiently expand the dataset

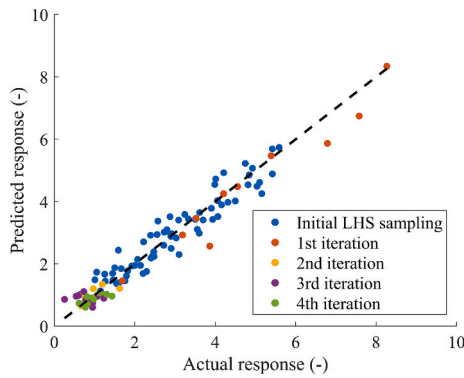


**Fig. 13.** Actual vs. predicted responses (i.e. weighted sum of relative errors as defined in Eq. (7)) during the surrogate model development process using adaptive sampling.

**Table 7**

Performance of the SM across adaptive sampling iterations, shown as the [mean  $\pm$  standard deviation] of  $R^2$  from 5 seed runs).

| Iteration            | Number of data points | $R^2$ of the SM |
|----------------------|-----------------------|-----------------|
| Initial LHS sampling | 70                    | $0.84 \pm 0.01$ |
| 1st iteration        | 80                    | $0.88 \pm 0.03$ |
| 2nd iteration        | 90                    | $0.92 \pm 0.01$ |
| 3rd iteration        | 100                   | $0.93 \pm 0.01$ |
| 4th iteration        | 110                   | $0.95 \pm 0.01$ |

by focusing on the most informative regions. As a result, the accuracy of the SM is improved while minimising computational costs.

### 3.5. Optimisation algorithm

We employed the Genetic Algorithm (GA) to efficiently optimise the surrogate model. GA is a population-based optimisation technique inspired by the principle of natural selection and genetics [53]. GA was chosen as it is well-suited for solving complex, high-dimensional, and non-linear optimisation problems where traditional gradient-based methods may struggle [12,54]. However, a common drawback of GA is its slow convergence and the high number of objective function evaluations required [54]. In our study, this limitation is mitigated by using a fast surrogate model instead of computationally expensive DEM simulations during the optimisation process. The parameters of GA are listed in Table A.3.

We executed the GA to search for a global minimum. Basically, it searches for DEM parameter sets that minimise the objective function—the weighted sum of the relative errors between experimental and DEM measurements for all KPIs. We performed the optimisation using two approaches:

- 1) Restricted optimisation: The GA was constrained to search for DEM parameter values below 0.9, as higher values are not reported for sinter and pellets in the literature [31].
- 2) Unrestricted optimisation: The GA was permitted to search the entire parameter space.

The results of both approaches, including the two best-performing parameter sets from each, are presented in Table 8. Since the optimised DEM parameters show negligible differences, we proceed with the results from the restricted optimisation.

The surrogate model inherently contains some stochasticity, which may lead to slight variations in its predictions. To take this variability into account, we trained the surrogate model 10 times and performed the GA optimisation separately for each trained model. In each run, we identified the parameter set with the minimum fitness value, i.e., the

**Table 8**

The results of the DEM calibration using the restricted and unrestricted genetic algorithms (GA).

| Parameters   | Restricted GA | Unrestricted GA |
|--------------|---------------|-----------------|
| $\mu_{s,pp}$ | 0.73          | 0.75            |
| $\mu_{r,pp}$ | 0.12          | 0.11            |
| $C_{r,pp}$   | 0.76          | 0.76            |
| $\mu_{s,ss}$ | 0.90          | 0.91            |
| $\mu_{s,pg}$ | 0.90          | 1.0             |
| $\mu_{r,pg}$ | 0.16          | 0.17            |
| $\mu_{s,sg}$ | 0.83          | 0.79            |

minimum weighted sum of errors. This process resulted in slightly different calibrated parameter sets, as shown in Table 9. However, since the variations between these sets were minimal, we selected only one parameter set with the lowest fitness value (run 4 in Table 9) as the final calibrated parameter set.

### 3.6. Verification of the calibrated parameters

To verify the calibration, we performed DEM simulations using the calibrated parameters highlighted in Table 9. Fig. 14 presents the relative errors between the experimental measurements and DEM results, calculated as  $\left(\frac{y_{DEM} - y_{Exp}}{y_{Exp}}\right) \times 100$ . The consistently low relative errors (all below 2 %) confirm the success of our calibration approach.

As shown in Fig. 7, bulk density in DEM is reassessed after calibration to ensure it matches the experimental bulk density. This is crucial because bulk density can be affected by particle-particle friction coefficients [45,55]. To achieve this, we used the maximum heap height in the lower box as a comparison metric. Fig. 15 shows that the heap height in DEM ( $H_{DEM}$ ) is lower than in the experiments ( $H_{Exp}$ ), indicating a higher bulk density in the DEM model.

To calibrate the bulk density, the particle density in DEM was adjusted by multiplying it by the ratio  $H_{DEM}/H_{Exp}$ . The average of this ratio across all the repetitions was calculated as 0.93. As a result, the calibrated particle densities for pellets and sinter were updated to 3350 ( $\text{kg/m}^3$ ) and 3208 ( $\text{kg/m}^3$ ), respectively.

We conducted a new set of DEM simulations using the calibrated particle densities. The results, presented in Fig. 16, show that the errors for most KPIs remain low, confirming the effectiveness of our calibration approach. However, a noticeable increase in the error for the mass flow rate was observed after reducing the particle density. This outcome was anticipated, as the mass flow rate is highly sensitive to changes in particle density [56]. This finding highlights the importance of including particle density as a calibration parameter when an accurate modelling of mass flow rate is of interest. Incorporating particle density in the main calibration process would improve the model's ability to capture this behaviour more accurately.

Fig. 17 provides a visual comparison between the DEM simulations and experiments at different time instances, demonstrating a strong agreement throughout the discharging process. This showcases the model's ability to accurately capture the flow dynamics over time.

### 3.7. Validation of the calibrated parameters

To validate the robustness of the calibrated model developed for the 50–50 pellet-sinter mass ratio, we extended the simulations to three additional cases: 75–25 and 25–75 mass ratios as well as the reverse layering. In these validation simulations, the pellet-sinter interaction parameters were kept as the average of the pellet-pellet and sinter-sinter interaction parameters, consistent with the parameters used for the 50–50 mixture. The results of these simulations are presented in Fig. 18, demonstrating good agreement between the DEM results and the experimental measurements for all KPIs. The accuracy of the developed

**Table 9**

Results of the genetic algorithm optimisation across 10 repetitions of surrogate model training for DEM calibration. The selected parameter set with the lowest fitness value is shaded in green.

| Repetition | $\mu_{s,pp}$ | $\mu_{r,pp}$ | $C_{r,pp}$ | $\mu_{s,ss}$ | $\mu_{s,pg}$ | $\mu_{r,pg}$ | $\mu_{s,sg}$ | Fitness value (weighted sum of errors) |
|------------|--------------|--------------|------------|--------------|--------------|--------------|--------------|--|
| 1          | 0.73         | 0.12         | 0.76       | 0.9          | 0.9          | 0.16         | 0.83         | 0.5532                                 |
| 2          | 0.65         | 0.12         | 0.75       | 0.9          | 0.9          | 0.17         | 0.89         | 0.5975                                 |
| 3          | 0.62         | 0.11         | 0.72       | 0.9          | 0.89         | 0.2          | 0.9          | 0.5567                                 |
| 4          | 0.74         | 0.12         | 0.76       | 0.9          | 0.9          | 0.16         | 0.83         | 0.5475                                 |
| 5          | 0.62         | 0.12         | 0.72       | 0.9          | 0.88         | 0.19         | 0.9          | 0.5676                                 |
| 6          | 0.69         | 0.12         | 0.76       | 0.9          | 0.9          | 0.17         | 0.85         | 0.5724                                 |
| 7          | 0.65         | 0.12         | 0.75       | 0.9          | 0.9          | 0.17         | 0.88         | 0.595                                  |
| 8          | 0.62         | 0.12         | 0.73       | 0.9          | 0.87         | 0.18         | 0.9          | 0.5856                                 |
| 9          | 0.74         | 0.12         | 0.76       | 0.9          | 0.9          | 0.16         | 0.83         | 0.5579                                 |
| 10         | 0.62         | 0.12         | 0.73       | 0.9          | 0.88         | 0.18         | 0.9          | 0.5811                                 |

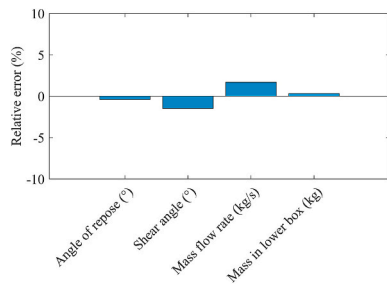


**Fig. 14.** DEM calibration results, showing the relative error between experimental measurements and DEM results for each KPI. The exact values of DEM results are provided in Table A.4.

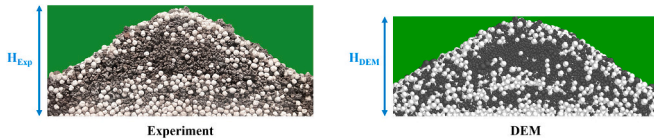


**Fig. 15.** Comparison of the height of the heap in the lower box between the experiment and DEM.

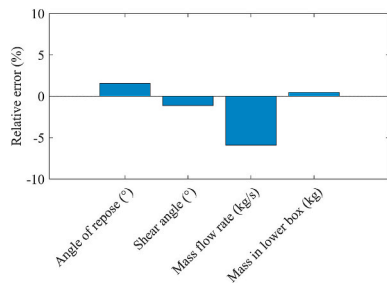


**Fig. 16.** DEM calibration results with calibrated particle density, showing the relative error between experimental measurements and DEM results for each KPI. The exact values of DEM results are provided in Table A.5.

DEM model for different mass ratios and layering orders confirms the generalisability and reliability of the calibrated parameters.

#### 4. Conclusion

In this study, we proposed an efficient and systematic calibration framework for DEM modelling of multi-component mixtures. We successfully applied the calibration framework to pellet-sinter mixtures, which are used in blast furnace steelmaking. The framework integrates sensitivity analysis based on definitive screening design (DSD), ML-based surrogate modelling using Gaussian process regression (GPR) with adaptive sampling, and optimisation techniques using genetic algorithms (GA) to minimise the number of required DEM simulations. The main findings can be summarised as follows:

- The proposed framework achieved a high-accuracy surrogate model ( $R^2$  of 0.95) for 7 DEM parameters using only 110 data points. This represents a 25 %–82 % reduction in dataset size compared to previous studies [27,57], while also achieving higher accuracy. These results highlight the efficiency of our framework in minimising computational costs while maintaining robust performance.
- Calibrated parameters for a 50–50 pellet-sinter mass ratio were valid across the other tested mass ratios and the reverse layering order. This suggests that, within the tested conditions, calibrating DEM parameters for one mass ratio and layering order is sufficient, eliminating the need for re-calibration of DEM parameters for different mixture ratios and layering configurations.
- Recalibrating the particle density at the end of the calibration process introduced errors in predicting the mass flow rate, while the errors for other KPIs remained low. This highlights the importance of actively calibrating particle density when dynamic processes are targeted.
- Interaction parameters for two-component mixtures can be effectively estimated as the average of the coefficients for the individual materials.
- Sensitivity analysis is a crucial step in calibrating a DEM model. It not only reduces the number of parameters to be calibrated but also reveals the sensitivity and relationship of KPIs to the DEM parameters. This insight helps determine whether certain KPIs are suitable for calibrating specific parameters. Moreover, it assists in defining an appropriate parameter space.
- Applying variance decomposition to the sensitivity analysis results revealed that the change in segregation, both in horizontal and vertical directions, is mostly caused by DEM stochasticity, hence no meaningful conclusion about the sensitivity of segregation to any



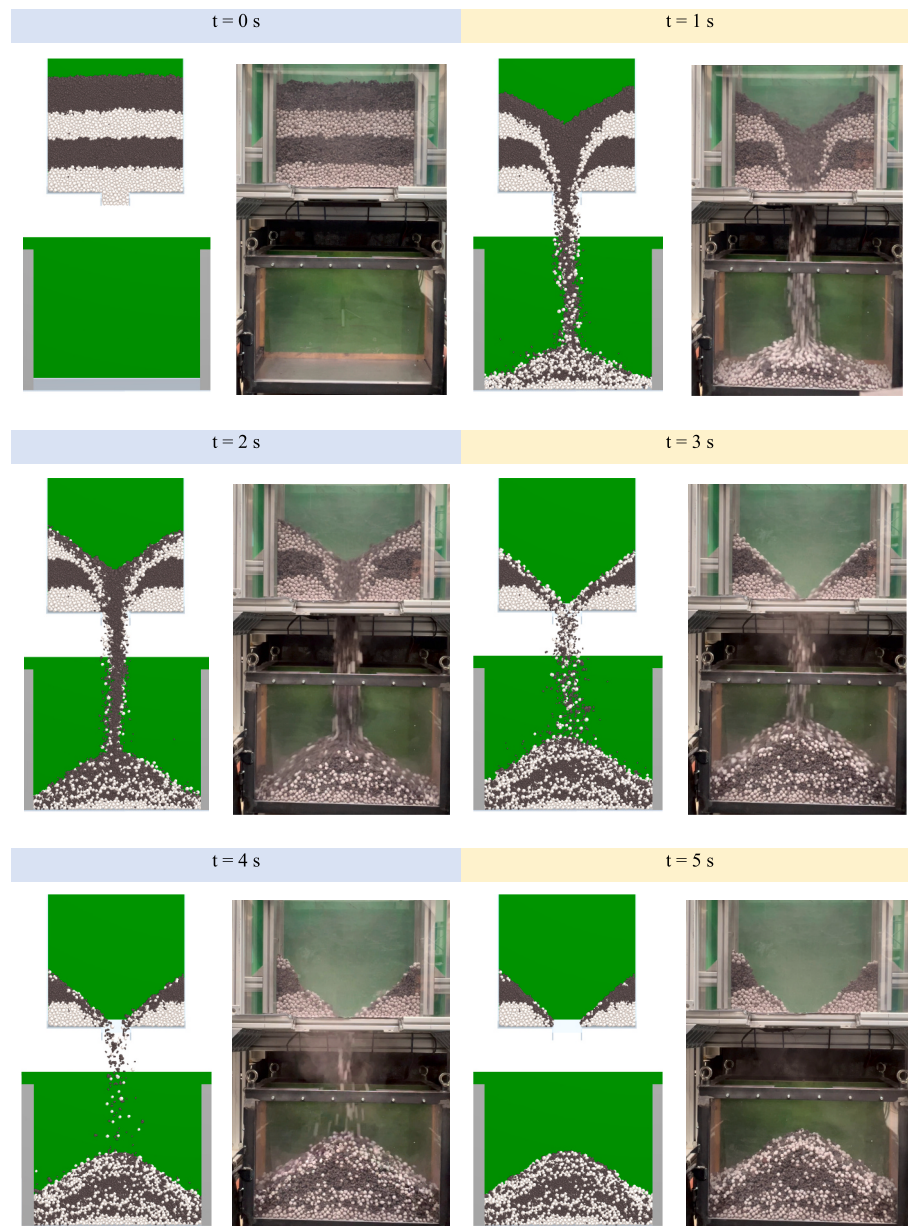


**Fig. 17.** Visual comparison between DEM and experiments at different time instances during the discharge process.

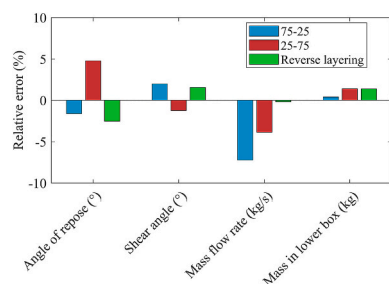


**Fig. 18.** Validation of the calibrated DEM parameters, showing the relative error between experimental measurements and DEM results for 75–25 and 25–75 pellet-sinter mass ratio, as well as the reverse layering case. The exact values of DEM results are provided in [Table A.6](#).

DEM parameter can be drawn. Therefore, the segregation measured in the draw down test, cannot be used for calibration.

The proposed calibration framework shows great promise for calibrating two-component mixtures with high efficiency and accuracy. Future work should focus on extending this approach to three or more components, incorporating additional KPIs, and exploring more advanced machine learning techniques to further improve calibration performance. Furthermore, validation across a broader range of test conditions is needed to assess the generalisability of the findings and reinforce the applicability to more complex granular systems.

#### CRediT authorship contribution statement

**Ahmed Hadi:** Writing – review & editing, Writing – original draft, Visualization, Validation, Software, Methodology, Investigation, Formal analysis, Conceptualization. **Yusong Pang:** Writing – review & editing, Visualization, Supervision, Project administration. **Dingena Schott:**

Writing – review & editing, Visualization, Validation, Supervision, Software, Resources, Project administration, Methodology, Investigation, Funding acquisition, Formal analysis, Conceptualization.

#### Declaration of competing interest

The authors declare that they have no known competing financial interests or personal relationships that could have appeared to influence the work reported in this paper

#### Acknowledgement

This research was carried out under project number T18019 in the framework of the Research Program of the Materials innovation institute (M2i) ([www.m2i.nl](http://www.m2i.nl)) supported by the Dutch government.

The authors would like to acknowledge ir. Jan van der Stel and dr.ir. Allert Adema from Tata Steel IJmuiden for supplying the experimental materials and the insightful discussions.

#### Appendix A. Appendix

**Table A.1**

Definitive screening design matrix.

| Run | $\mu_{s,pp}$ | $\mu_{r,pp}$ | $C_{r,pp}$ | $\mu_{s,ss}$ | $\mu_{r,ss}$ | $C_{r,ss}$ | $\mu_{s,pg}$ | $\mu_{r,pg}$ | $C_{r,pg}$ | $\mu_{s,sg}$ | $\mu_{r,sg}$ | $C_{r,sg}$ |
|-----|--------------|--------------|------------|--------------|--------------|------------|--------------|--------------|------------|--------------|--------------|------------|
| 1   | 0.613        | 0.06         | 0.525      | 0.525        | 0.1          | 0.263      | 0.285        | 0.045        | 0.875      | 0.475        | 0.1          | 0.3        |
| 2   | 0.4905       | 0.045        | 0.525      | 0.525        | 0.06         | 0.263      | 0.285        | 0.045        | 0.525      | 0.285        | 0.06         | 0.3        |
| 3   | 0.4905       | 0.075        | 0.875      | 0.875        | 0.1          | 0.438      | 0.475        | 0.075        | 0.875      | 0.475        | 0.1          | 0.5        |
| 4   | 0.368        | 0.045        | 0.875      | 0.875        | 0.08         | 0.438      | 0.285        | 0.045        | 0.525      | 0.475        | 0.1          | 0.3        |
| 5   | 0.368        | 0.075        | 0.875      | 0.525        | 0.1          | 0.263      | 0.475        | 0.045        | 0.525      | 0.285        | 0.1          | 0.3        |
| 6   | 0.613        | 0.075        | 0.525      | 0.875        | 0.1          | 0.438      | 0.475        | 0.075        | 0.525      | 0.475        | 0.06         | 0.3        |
| 7   | 0.368        | 0.045        | 0.875      | 0.875        | 0.06         | 0.263      | 0.475        | 0.075        | 0.7        | 0.475        | 0.1          | 0.3        |
| 8   | 0.613        | 0.045        | 0.875      | 0.525        | 0.06         | 0.3505     | 0.285        | 0.075        | 0.875      | 0.475        | 0.06         | 0.3        |
| 9   | 0.613        | 0.045        | 0.7        | 0.525        | 0.06         | 0.438      | 0.475        | 0.045        | 0.525      | 0.475        | 0.1          | 0.5        |
| 10  | 0.368        | 0.045        | 0.525      | 0.875        | 0.1          | 0.263      | 0.285        | 0.075        | 0.875      | 0.38         | 0.1          | 0.5        |
| 11  | 0.613        | 0.075        | 0.525      | 0.525        | 0.08         | 0.263      | 0.475        | 0.075        | 0.875      | 0.285        | 0.06         | 0.5        |
| 12  | 0.613        | 0.045        | 0.525      | 0.875        | 0.1          | 0.438      | 0.285        | 0.06         | 0.525      | 0.285        | 0.1          | 0.3        |
| 13  | 0.613        | 0.075        | 0.525      | 0.875        | 0.06         | 0.263      | 0.475        | 0.045        | 0.875      | 0.475        | 0.1          | 0.3        |
| 14  | 0.368        | 0.075        | 0.875      | 0.7          | 0.1          | 0.438      | 0.285        | 0.045        | 0.875      | 0.475        | 0.06         | 0.3        |
| 15  | 0.368        | 0.075        | 0.525      | 0.525        | 0.06         | 0.438      | 0.38         | 0.075        | 0.875      | 0.285        | 0.1          | 0.3        |
| 16  | 0.613        | 0.045        | 0.875      | 0.525        | 0.1          | 0.438      | 0.475        | 0.075        | 0.875      | 0.285        | 0.1          | 0.3        |
| 17  | 0.613        | 0.045        | 0.525      | 0.7          | 0.06         | 0.263      | 0.475        | 0.075        | 0.525      | 0.285        | 0.1          | 0.5        |
| 18  | 0.613        | 0.045        | 0.525      | 0.875        | 0.06         | 0.438      | 0.285        | 0.075        | 0.875      | 0.475        | 0.06         | 0.5        |
| 19  | 0.368        | 0.045        | 0.525      | 0.525        | 0.1          | 0.438      | 0.475        | 0.045        | 0.875      | 0.475        | 0.08         | 0.5        |
| 20  | 0.368        | 0.045        | 0.525      | 0.875        | 0.06         | 0.438      | 0.475        | 0.045        | 0.875      | 0.285        | 0.06         | 0.3        |
| 21  | 0.613        | 0.075        | 0.875      | 0.875        | 0.06         | 0.438      | 0.285        | 0.045        | 0.875      | 0.285        | 0.1          | 0.5        |
| 22  | 0.368        | 0.075        | 0.525      | 0.525        | 0.06         | 0.438      | 0.285        | 0.075        | 0.525      | 0.475        | 0.1          | 0.4        |
| 23  | 0.368        | 0.045        | 0.875      | 0.525        | 0.06         | 0.263      | 0.285        | 0.045        | 0.875      | 0.285        | 0.1          | 0.5        |
| 24  | 0.368        | 0.075        | 0.7        | 0.875        | 0.1          | 0.263      | 0.285        | 0.075        | 0.875      | 0.285        | 0.06         | 0.3        |
| 25  | 0.613        | 0.075        | 0.875      | 0.525        | 0.1          | 0.263      | 0.285        | 0.075        | 0.525      | 0.475        | 0.1          | 0.5        |
| 26  | 0.368        | 0.045        | 0.875      | 0.525        | 0.1          | 0.438      | 0.285        | 0.075        | 0.525      | 0.285        | 0.06         | 0.5        |
| 27  | 0.613        | 0.045        | 0.875      | 0.875        | 0.1          | 0.263      | 0.475        | 0.045        | 0.875      | 0.285        | 0.06         | 0.4        |
| 28  | 0.613        | 0.075        | 0.525      | 0.525        | 0.1          | 0.438      | 0.285        | 0.045        | 0.7        | 0.285        | 0.06         | 0.5        |
| 29  | 0.368        | 0.075        | 0.875      | 0.525        | 0.06         | 0.263      | 0.475        | 0.06         | 0.875      | 0.475        | 0.06         | 0.5        |

**Table A.2**

Kernel functions of GPR and the relevant equations.

| Kernel name         | Kernel function ( $k(x, x')$ )  |
|---------------------|---|
| Exponential         | $\sigma_f^2 \exp\left(-\frac{r}{\sigma_l}\right)$                                   |
| Squared exponential | $\sigma_f^2 \exp\left[-\frac{1}{2} \frac{r^2}{\sigma_l^2}\right]$                   |
| Rational quadratic  | $\sigma_f^2 \left(1 + \frac{r^2}{2\alpha\sigma_l^2}\right)^{-\alpha}$               |
| Matern 5/2          | $\sigma_f^2 \left(1 + \frac{\sqrt{5}r}{\sigma_l} + \frac{5r^2}{3\sigma_l^2}\right)$ |

$r = \sqrt{(x - x')^T (x - x')}$  is Euclidean distance between  $x$  and  $x'$ .

$\sigma_f^2$  is the signal variance of the function  $f$ .

$\sigma_l$  is the characteristic length scale.

$\alpha$  is a positive-valued scale-mixture parameter.

**Table A.3**

Parameters used for genetic algorithm.

| Parameter                  | Value | Description   |
|----------------------------|-------|---|
| Population size            | 1000  | Number of individuals in each generation.                                   |
| Max. number of generations | 2000  | Maximum number of generations for algorithm to solve.                       |
| Crossover probability      | 0.6   | The proportion of the population selected for crossover in each generation. |
| Mutation probability       | 0.05  | Mutation fraction used to introduce diversity into the population.          |
| Function Tolerance         | 1e-6  | Stopping criterion based on the minimal improvement in fitness function.    |

**Table A.4**

DEM calibration results for 50–50 pellet-sinter mass ratio, presenting the comparison between DEM results and experimental measurements, along with the relative errors for each KPI.

|                    | Angle of repose (°) | Shear angle (°) | Mass flow rate (kg/s) | Mass in the lower box (kg) |
|--------------------|---------------------|-----------------|-----------------------|----------------------------|
| Experiments        | 29.47 ± 0.48        | 42.51 ± 1.62    | 10.29 ± 0.35          | 32.32 ± 0.55               |
| DEM                | 29.36 ± 0.5         | 41.88 ± 0.93    | 10.46 ± 0.11          | 32.43 ± 0.19               |
| Relative error (%) | −0.38               | −1.48           | 1.67                  | 0.33                       |

**Table A.5**

DEM calibration results for 50–50 pellet-sinter mass ratio with calibrated particle density, presenting the comparison between DEM results and experimental measurements, along with the relative errors for each KPI.

|                    | Angle of repose (°) | Shear angle (°) | Mass flow rate (kg/s) | Mass in the lower box (kg) |
|--------------------|---------------------|-----------------|-----------------------|----------------------------|
| Experiments        | 29.47 ± 0.48        | 42.51 ± 1.62    | 10.29 ± 0.35          | 32.32 ± 0.55               |
| DEM                | 29.93 ± 0.62        | 42.03 ± 1.08    | 9.68 ± 0.08           | 32.47 ± 0.06               |
| Relative error (%) | 1.56                | −1.12           | −5.91                 | 0.46                       |

**Table A.6**

Validation result of the calibrated DEM parameters for 75–25 and 25–75 pellet-sinter mass ratios as well as the reverse layering order, presenting the comparison between DEM results and experimental measurements, along with the relative errors for each KPI.

| Case    |                    | Angle of repose (°) | Shear angle (°) | Mass flow rate (kg/s) | Mass in the lower box (kg) |
|---------|--------------------|---------------------|-----------------|-----------------------|----------------------------|
| 75–25   | Experiments        | 28.55 ± 0.65        | 39.03 ± 1.49    | 10.29 ± 0.1           | 33.09 ± 0.12               |
|         | DEM                | 28.09 ± 0.48        | 39.81 ± 1.71    | 9.55 ± 0.12           | 33.22 ± 0.16               |
|         | Relative error (%) | −1.60               | 1.99            | −7.23                 | 0.39                       |
| 25–75   | Experiments        | 29.63 ± 0.75        | 44.76 ± 1.21    | 10.24 ± 0.45          | 32.00 ± 0.48               |
|         | DEM                | 31.04 ± 0.34        | 44.21 ± 0.56    | 9.84 ± 0.12           | 32.45 ± 0.08               |
|         | Relative error (%) | 4.76                | −1.23           | −3.87                 | 1.39                       |
| Reverse | Experiments        | 29.74 ± 0.47        | 40.92 ± 1.55    | 10.39 ± 0.56          | 32.97 ± 0.2                |
|         | DEM                | 28.99 ± 0.34        | 41.55 ± 0.67    | 10.37 ± 0.18          | 33.42 ± 0.12               |
|         | Relative error (%) | −2.52               | 1.54            | −0.17                 | 1.37                       |

## Data availability

I have shared a link to the dataset.

## References

- [1] P. Richard, M. Nicodemi, R. Delannay, P. Ribière, D. Bideau, Slow relaxation and compaction of granular systems, *Nat. Mater.* 4 (2005) 121–128, <https://doi.org/10.1038/nmat1300>.
- [2] P.A. Cundall, O.D.L. Strack, A discrete numerical model for granular assemblies, *Geotechnique* 29 (1979) 47–65, <https://doi.org/10.1680/geot.1979.29.1.47>.
- [3] C. Wellmann, P. Wriggers, A two-scale model of granular materials, *Comput. Methods Appl. Mech. Eng.* 205 (2012) 46–58.
- [4] C. Yuan, B. Chareyre, A pore-scale method for hydromechanical coupling in deformable granular media, *Comput. Methods Appl. Mech. Eng.* 318 (2017) 1066–1079.
- [5] J. Emmerink, A. Hadi, J. Jovanova, C. Cleven, D.L. Schott, Parametric analysis of a double shaft, batch-type paddle mixer using the discrete element method (DEM), *Processes* 11 (2023), <https://doi.org/10.3390/pr11030738>.
- [6] S. Ren, P. Zhang, Y. Zhao, X. Tian, S.A. Galindo-Torres, A coupled metaball discrete element material point method for fluid–particle interactions with free surface flows and irregular shape particles, *Comput. Methods Appl. Mech. Eng.* 417 (2023) 116440.
- [7] S. Nadimi, A. Ghanbarzadeh, A. Neville, M. Ghadiri, Effect of particle roughness on the bulk deformation using coupled boundary element and discrete element methods, *Comput. Part. Mech.* (2019) 1–11.
- [8] F. Mostafaei, C. Davies, M. Wong, R. Turki, P. Liu, A. Sarkar, P. Doshi, J.G. Khinast, D. Jajcevic, Analysis of powder behaviour in bin blending processes at different scales using DEM, *Adv. Powder Technol.* 34 (2023) 104166.
- [9] A. Hadi, M. Moradi, Y. Pang, D. Schott, Adaptive AI-based surrogate modelling via transfer learning for DEM simulation of multi-component segregation, *Sci. Rep.* 14 (2024) 27003.
- [10] S.J. Lee, Y.M.A. Hashash, E.G. Nezami, Simulation of triaxial compression tests with polyhedral discrete elements, *Comput. Geotech.* 43 (2012) 92–100, <https://doi.org/10.1016/j.compgeo.2012.02.011>.
- [11] H. Huang, E. Tutumluer, Discrete element modeling for fouled railroad ballast, *Constr. Build. Mater.* 25 (2011) 3306–3312, <https://doi.org/10.1016/j.conbuildmat.2011.03.019>.
- [12] C. Richter, T. Rößler, G. Kunze, A. Katterfeld, F. Will, Development of a standard calibration procedure for the DEM parameters of cohesionless bulk materials – part II: efficient optimization-based calibration, *Powder Technol.* 360 (2020) 967–976, <https://doi.org/10.1016/j.powtec.2019.10.052>.
- [13] G. Heß, C. Richter, A. Katterfeld, Simulation of the dynamic interaction between bulk material and heavy equipment: Calibration and validation, in: *ICBMH 2016 -*

- 12th International Conference on Bulk Materials Storage, Handling and Transportation, Proceedings, 2016, pp. 427–436.
- [14] M.J. Mohajeri, H.Q. Do, D.L. Schott, DEM calibration of cohesive material in the ring shear test by applying a genetic algorithm framework, *Adv. Powder Technol.* 31 (2020) 1838–1850, <https://doi.org/10.1016/j.apt.2020.02.019>.
- [15] H.Q. Do, A.M. Aragón, D.L. Schott, A calibration framework for discrete element model parameters using genetic algorithms, *Adv. Powder Technol.* 29 (2018) 1393–1403, <https://doi.org/10.1016/j.apt.2018.03.001>.
- [16] H. Shi, C. Cengiz, G. Macaro, M. Martinelli, J. Jovanova, D. Schott, A validated DEM modelling framework on plate and pile penetrations in a double-layer scour protection system, *Ocean Eng.* 319 (2025) 120222.
- [17] M.P. Fransen, M. Langelaar, D.L. Schott, Application of DEM-based metamodelling in bulk handling equipment design: methodology and DEM case study, *Powder Technol.* 393 (2021) 205–218, <https://doi.org/10.1016/j.powtec.2021.07.048>.
- [18] M. Rackl, K.J. Hanley, A methodical calibration procedure for discrete element models, *Powder Technol.* 307 (2017) 73–83, <https://doi.org/10.1016/j.powtec.2016.11.048>.
- [19] J. Grobbel, S. Brendelberger, M. Henninger, C. Sattler, R. Pitz-Paal, Calibration of parameters for DEM simulations of solar particle receivers by bulk experiments and surrogate functions, *Powder Technol.* 364 (2020) 831–844, <https://doi.org/10.1016/j.powtec.2019.11.028>.
- [20] J. De Pue, G. Di Emidio, R.D. Verastegui Flores, A. Bezuijen, W.M. Cornelis, calibration of DEM material parameters to simulate stress-strain behaviour of unsaturated soils during uniaxial compression, *Soil Tillage Res.* 194 (2019), <https://doi.org/10.1016/j.still.2019.104303>.
- [21] M.P. Fransen, M. Langelaar, D.L. Schott, Including stochastics in metamodel-based DEM model calibration, *Powder Technol.* 406 (2022), <https://doi.org/10.1016/j.powtec.2022.117400>.
- [22] F. Westbrink, A. Elbel, A. Schwung, S.X. Ding, Optimization of DEM parameters using multi-objective reinforcement learning, *Powder Technol.* 379 (2021) 602–616, <https://doi.org/10.1016/j.powtec.2020.10.067>.
- [23] H. Cheng, T. Shuku, K. Thoeni, P. Tempone, S. Luding, V. Magnanimo, An iterative Bayesian filtering framework for fast and automated calibration of DEM models, *Comput. Methods Appl. Mech. Eng.* 350 (2019) 268–294, <https://doi.org/10.1016/j.cma.2019.01.027>.
- [24] P. Hartmann, H. Cheng, K. Thoeni, Performance study of iterative Bayesian filtering to develop an efficient calibration framework for DEM, *Comput. Geotech.* 141 (2022), <https://doi.org/10.1016/j.compgeo.2021.104491>.
- [25] B. El-Kassem, N. Salloum, T. Brinz, Y. Heider, B. Markert, A multivariate regression parametric study on DEM input parameters of free-flowing and cohesive powders with experimental data-based validation, *Comput. Part. Mech.* 8 (2021) 87–111, <https://doi.org/10.1007/s40571-020-00315-8>.
- [26] L. Benvenuti, C. Kloss, S. Pirker, Identification of DEM simulation parameters by artificial neural networks and bulk experiments, *Powder Technol.* 291 (2016) 456–465, <https://doi.org/10.1016/j.powtec.2016.01.003>.
- [27] J. Irazábal, F. Salazar, D.J. Vicente, A methodology for calibrating parameters in discrete element models based on machine learning surrogates, *Comput. Part. Mech.* 10 (2023) 1031–1047, <https://doi.org/10.1007/s40571-022-00550-1>.
- [28] A.H. Hadi, Y. Pang, D.L. Schott, Calibration of DEM parameters for multi-component segregation, in: ICBMH 2023: 14th International Conference on Bulk Materials Storage, Handling and Transportation, 2023.
- [29] Y. Hu, Y. Lu, A novel framework for calibrating DEM parameters: a case study of sand and soil-rock mixture, *Comput. Geotech.* 174 (2024) 106619.
- [30] R. van Sleetuwen, S. Pantaleev, M. Ebrahimi, Efficient DEM modeling of solid flavor particle mixing in a rotary drum, *Powder Technol.* 437 (2024) 119559.
- [31] A. Hadi, H. Shi, Y. Pang, D. Schott, Identification of dominant DEM parameters for multi-component segregation during heap formation, hopper discharge and chute flow, *Powder Technol.* 444 (2024) 119985.
- [32] J.G. Wasserfall, C.J. Coetzee, C.J. Meyer, A submerged draw down test calibration method for fully-coupled CFD-DEM modelling, *Front. Chem. Eng.* 6 (2024) 1376974.
- [33] T. Roessler, C. Richter, A. Katterfeld, F. Will, Development of a standard calibration procedure for the DEM parameters of cohesionless bulk materials – part I: solving the problem of ambiguous parameter combinations, *Powder Technol.* 343 (2019) 803–812, <https://doi.org/10.1016/j.powtec.2018.11.034>.
- [34] C. Ramírez-Aragón, F. Alba-Elías, A. González-Marcos, J. Ordieres-Meré, Segregation in the tank of a rotary tablet press machine using experimental and discrete element methods, *Powder Technol.* 328 (2018) 452–469.
- [35] B. Jian, X. Gao, Investigation of spherical and non-spherical binary particles flow characteristics in a discharge hopper, *Adv. Powder Technol.* 34 (2023) 104011.
- [36] H.M. Beakawi Al-Hashemi, O.S. Baghabra Al-Amoudi, A review on the angle of repose of granular materials, *Powder Technol.* 330 (2018) 397–417, <https://doi.org/10.1016/j.powtec.2018.02.003>.
- [37] A. Hadi, R. Roepal, Y. Pang, D.L. Schott, DEM modelling of segregation in granular materials: a review, *Kona Powder Part. J.* (2023), <https://doi.org/10.14356/kona.2024017>.
- [38] M. Asachi, E. Nourafkan, A. Hassanpour, A review of current techniques for the evaluation of powder mixing, *Adv. Powder Technol.* 29 (2018) 1525–1549, <https://doi.org/10.1016/j.apt.2018.03.031>.
- [39] A. Hadi, Y. Pang, D. Schott, Experimental Data on Pellet-Sinter Mixtures in Draw Down Tests, 4TU. Research Data, 2025, <https://doi.org/10.4121/2daf34e0-5858-4eab-a891-ceed28e55f5f.v1>.
- [40] A. Chakrabarty, R. Biswas, S. Basu, S. Nag, Characterisation of binary mixtures of pellets and sinter for DEM simulations, *Adv. Powder Technol.* 33 (2022), <https://doi.org/10.1016/j.apt.2021.11.010>.
- [41] J. Ai, J.F. Chen, J.M. Rotter, J.Y. Ooi, Assessment of rolling resistance models in discrete element simulations, *Powder Technol.* 206 (2011) 269–282, <https://doi.org/10.1016/j.powtec.2010.09.030>.
- [42] A. Tripathi, V. Kumar, A. Agarwal, A. Tripathi, S. Basu, A. Chakrabarty, S. Nag, Quantitative DEM simulation of pellet and sinter particles using rolling friction estimated from image analysis, *Powder Technol.* 380 (2021) 288–302, <https://doi.org/10.1016/j.powtec.2020.11.024>.
- [43] H.P. Zhu, Z.Y. Zhou, R.Y. Yang, A.B. Yu, Discrete particle simulation of particulate systems: theoretical developments, *Chem. Eng. Sci.* 62 (2007) 3378–3396, <https://doi.org/10.1016/j.ces.2006.12.089>.
- [44] E. Izard, M. Moreau, P. Ravier, Discrete element method simulation of segregation pattern in a sinter cooler charging chute system, *Particuology* 59 (2021) 34–42, <https://doi.org/10.1016/j.partic.2020.08.004>.
- [45] C.J. Coetzee, Review: calibration of the discrete element method, *Powder Technol.* 310 (2017) 104–142, <https://doi.org/10.1016/j.powtec.2017.01.015>.
- [46] B. Jones, C.J. Nachtsheim, A class of three-level designs for definitive screening in the presence of second-order effects, *J. Qual. Technol.* 43 (2011) 1–15, <https://doi.org/10.1080/00224065.2011.11917841>.
- [47] B. Jones, C.J. Nachtsheim, Effective design-based model selection for definitive screening designs, *Technometrics* 59 (2017) 319–329, <https://doi.org/10.1080/00401706.2016.1234979>.
- [48] N.A. Weiss, P.T. Holmes, M. Hardy, *A Course in Probability*, Pearson Addison Wesley Boston, MA, USA, 2006.
- [49] J.L. Loepky, J. Sacks, W.J. Welch, Choosing the sample size of a computer experiment: a practical guide, *Technometrics* 51 (2009) 366–376.
- [50] H. Liu, Y.-S. Ong, J. Cai, A survey of adaptive sampling for global metamodeling in support of simulation-based complex engineering design, *Struct. Multidiscip. Optim.* 57 (2018) 393–416.
- [51] D.R. Jones, M. Schonlau, W.J. Welch, Efficient global optimization of expensive black-box functions, *J. Glob. Optim.* 13 (1998) 455–492.
- [52] J.N. Fuhg, A. Fau, U. Nackenhorst, State-of-the-art and comparative review of adaptive sampling methods for kriging, *Arch. Comput. Methods Eng.* 28 (2021) 2689–2747.
- [53] D.E. Goldberg, *Genetic Algorithms in Search, Optimization, and Machine Learning* 1989, Addison Wesley, 1989, p. 36.
- [54] H.-G. Beyer, B. Sendhoff, Robust optimization—a comprehensive survey, *Comput. Methods Appl. Mech. Eng.* 196 (2007) 3190–3218.
- [55] B. Majidi, K. Azari, H. Alamdari, M. Fafard, D. Ziegler, Simulation of vibrated bulk density of anode-grade coke particles using discrete element method, *Powder Technol.* 261 (2014) 154–160.
- [56] A. Katterfeld, C. Coetzee, T. Donohue, J. Fottner, A. Grima, A. Ramirez Gomez, D. Ilıc, R. Kačianauskas, J. Necas, D. Schott, Calibration of DEM Parameters for Cohesionless Bulk Materials Under Rapid Flow Conditions and Low Consolidation, White Paper, 2019.
- [57] C. Xu, X. Liu, E. Wang, S. Wang, Calibration of the microparameters of rock specimens by using various machine learning algorithms, *Int. J. Geomech.* 21 (2021) 04021060.